Cavity Flow in Scramjet Engine by Space–Time Conservation and Solution Element Method

Chang-Kee Kim,* S.-T. John Yu,† and Zeng-Chan Zhang‡
The Ohio State University, Columbus, Ohio 43210-1154

Numerical simulation of supersonic flows over open cavities in the setting of a dual-mode ramjet/scramjet engine are reported. To calculate the unsteady cavity flows, we employ the space–time conservation element and solution element (CESE) method, a novel numerical method based on a unified treatment of space and time for calculation of flux balance. Supersonic cavity flows with and without fuel injection are studied to understand the mechanisms of mixing enhancement and flame holding by cavities. Without injection, numerical results compared favorably with the experimental data for dominant frequencies and time-averaged pressure coefficients inside the cavities. With an upstream injection, the flow oscillations are drastically suppressed. In a downstream injection arrangement, cavity-generated acoustic waves and vortices greatly enhance fuel/air mixing. Numerical results show that the CESE method provides high-fidelity numerical results of unsteady flows in the advanced scramjet engine concept.

I. Introduction

FUEL injection, ignition, and flameholding are challenging issues for high-speed combustion. In a viable scramjet engine, the fuel injection method employed must provide rapid fuel/air mixing with minimum total-pressure loss in the airstream. A stable flameholding system under a wide range of operating conditions is critical to sustain the supersonic combustion. Recently, cavity-based flameholders, an integrated mixing-enhancement and flameholding approach, have attracted considerable attention in the scramjet community. Under suitable conditions, flow recirculation, or the trapped vortices, significantly increases the flow residence time of the fluid entering the cavity. A pilot flame could be set up inside the cavity to provide a pool of hot chemical radicals, which in turn would reduce the ignition delay of the air/fuel mixture in the airstream and, thus, sustain high-speed combustion.

High-speed cavity flows are inherently unsteady, involving both broadband small-scale fluctuations typical of turbulent flows, as well as distinct resonance with harmonic properties in its frequencies and amplitudes. In the past, it has been demonstrated that the aspect ratio of the cavity and freestream flow conditions are the critical parameters dominating the complex flow features, including boundary-layer separation, compressible free shear layer with shedding vortices, linear/nonlinear acoustic waves, and complex shock and expansion waves interacting with vortices and acoustic waves.

In the setting of wheel wells and bomb bays, previous studies for high-speed cavity flows showed that cavity flows could be categorized into the following two groups: 1) open cavity flows, when $L/D < 7 \sim 10$, and 2) closed cavity flows, when $L/D > 7 \sim 10$, where L denotes the length of the cavity and D the depth. In flows over cavities of large aspect ratios ($L/D > 7 \sim 10$), the separated free shear layer emanating from the upstream corner of the cavity reattaches to the bottom wall of the cavity and results in two separated recirculation zones near the two corners between the lateral walls and the cavity floor. The resultant low-pressure zones at the lower corners and high pressures on the cavity floor, where the shear layer reattaches, lead to significant drag and pressure loss of the airstream. In this case, mass addition/ejection into/from the cavity by aerodynamic unsteadiness is low to moderate, and the flow is referred to as closed.

On the other hand, flows over cavities with smaller aspect ratios, $L/D < 7 \sim 10$, result in reattachment of the free shear layer to the rear bulkhead of the cavity. The impingement of the free shear layer on the rear lateral wall causes violent unsteady motions and results in significant periodical mass addition/ejection near the rear bulkhead of the cavity. These flows are referred to as open. The wave patterns of open cavity flows could be further categorized into 1) transverse mode for very short cavities, $L/D \cong 1$, and 2) longitudinal mode for longer cavities, for example, $2 \sim 3 < L/D < 7 \sim 10$. In short cavities, $L/D < 2$, only one main vortex inside the cavity is sustained by the driving shear layer spanning the top of the cavity. The up and down motions of the single main recirculation bubble generate acoustic waves, which by and large propagate in the direction perpendicular to the free shear layer, provided the freestream is transonic. The propagating waves are referred to as in a transverse mode. On the other hand, when the cavity is longer, $2 \sim 3 < L/D < 7 \sim 10$, multiple moving vortices occur inside the cavity leading to complex interactions among trapped vortices, propagating and rebounding pressure waves, and the flapping free shear layer. In general, the rebounding pressure waves, while interacting with the free shear layer, drastically amplify the growth rate of the free shear layer, which, in turn, sheds enormous vortices propagating toward and impinging on the aft wall of the cavity. Because of propagating vortices in the streamwise direction and the rebounding pressure waves, prevalent acoustic waves propagate in the longitudinal direction outside the cavity into the downstream area. If the airstream is transonic or subsonic, the acoustics would transversely propagate into the upstream areas.

In the setting of supersonic combustion inside a scramjet engine, trapped vortices inside cavities could be useful for flameholding. Moreover, cavity resonance, which produces periodic mass addition/expulsion with large flow structures, could be useful for mixing enhancement. Simultaneously, cavity drag must be minimal, for example, much less than that of a bluff body, and thereby only cause acceptable pressure loss. Gruber et al.[1,2] have developed a dual-mode ramjet/scramjet engine concept, which is envisioned to use hydrocarbon fuels for a flight regime of Mach numbers from 3 to $6 \sim 9$. In their supersonic combustors,[1,2] open cavities with aspect ratios about $5 < L/D < 8$ have been tested in conjunction with various fuel injection schemes. Numerical simulation of cavity flows

*Research Associate, Mechanical Engineering Department; currently Senior Scientist, Agency for Defense Development, Tech 3-7, Yuseong, P.O. Box 35-5, Daejon 305-600, Republic of Korea. Member AIAA.
†Associate Professor, Mechanical Engineering Department; yu.274@osu.edu. Member AIAA.
‡Research Associate, Mechanical Engineering Department; currently Senior Engineer, Livermore Software, 7374 Las Positas Road, Livermore, CA 94550. Member AIAA.

has been conducted by Baurle et al.[3] The results showed that the cavities have great potential to be a viable combined flameholder/mixing enhancement device for a scramjet engine combustor. Similar ideas have also been independently proposed and tested by Yu et al.[4] In particular, Yu et al.[4] have tested supersonic flows passing multiple cavities. Some of recent results have been summarized by Ben-Yakar and Hanson.[5]

In the past, extensive experimental and theoretical studies on cavity flows have been conducted for applications in wheel wells and bomb bays, and flow characteristics such as the oscillation frequency and amplitudes at various locations in the cavity have been reported.[6−11] However, it is difficult to apply this knowledge base directly to cavity flows for the advanced scramjet engines due to much shorter length/timescales in scramjet engines. Additional complexity associated with fuel injection also warrants further studies because cavity flows and the associated acoustics would be drastically changed by the fuel injection schemes employed. In particular, inherent oscillations of cavity flows may be significantly suppressed by an upstream injection.[4,9−11]

In the present paper, we focus on time-accurate calculation of supersonic cavity flows in the setting of a dual-mode ramjet/scramjet engine combustor.[1,2] The objectives of the present study are 1) to validate the numerical results by assessment of the calculated frequencies and amplitudes of pressure oscillations and comparison with previously reported data, 2) to assess the fuel/air mixing enhancement based on the application of upstream as well as downstream injection to cavity flows, and 3) to demonstrate the capabilities of the conservation element and solution element (CESE) method for capturing complex flow features of the supersonic cavity flows.

The rest of the paper is organized as follows. Section II is a review of the model equations to be solved by the CESE method. Section III provides background information on the CESE method. Section IV shows numerical solutions, including comparison between the numerical results and previously reported data. Moreover, we will show the effects by both upstream and downstream injection on pressure oscillations, acoustics, and vortices, leading to effects on fuel/air mixing and flameholding. We then offer concluding remarks and provide cited references.

II. Governing Equations

The fundamental behavior of cavity flows was known to be two-dimensional.[8] Equation (1) shows the vector form of the two-dimensional flow equations in Cartesian coordinates, including the continuity equation, the Navier–Stokes equations, the energy equation, and one species equation:

$$\frac{\partial U}{\partial t} + \frac{\partial F}{\partial x} + \frac{\partial G}{\partial y} - \frac{\partial F_v}{\partial x} - \frac{\partial G_v}{\partial y} = 0 \tag{1a}$$

where the flow variable vector

$$U = \begin{pmatrix} \rho \\ \rho u \\ \rho v \\ \rho e \\ \rho Y_f \end{pmatrix} \tag{1b}$$

the inviscid flux vectors are

$$F = \begin{pmatrix} \rho u \\ \rho u^2 + p \\ \rho uv \\ u(\rho e + p) \\ \rho u Y_f \end{pmatrix}, \qquad G = \begin{pmatrix} \rho v \\ \rho uv \\ \rho v^2 + p \\ v(\rho e + p) \\ \rho v Y_f \end{pmatrix} \tag{1c}$$

and the viscous flux vectors are

$$F_v = \begin{pmatrix} 0 \\ \tau_{xx} \\ \tau_{xy} \\ u\tau_{xx} + v\tau_{xy} - q_x \\ -\rho \hat{u}_f Y_f \end{pmatrix}, \qquad G_v = \begin{pmatrix} 0 \\ \tau_{xy} \\ \tau_{yy} \\ u\tau_{xy} + v\tau_{yy} - q_y \\ -\rho \hat{v}_f Y_f \end{pmatrix} \tag{1d}$$

In the preceding equations, ρ is the density; u and v are velocity components in the x and the y directions, respectively; p is the static pressure; and $e = \varepsilon + \frac{1}{2}(u^2 + v^2)$ is the specific total energy with ε as the specific internal energy. We assume the fluid is ideal and polytropic. Because of the equation of state of an ideal gas, $p = (\gamma - 1)\rho\varepsilon$, where $\gamma = C_p/C_v$ is the specific heat ratio, and it is a constant due to the polytropic gas assumption. In the viscous vectors, τ_{xx}, τ_{xy}, and τ_{yy} are stress components; and q_x and q_y are the heat conduction fluxes in the x and y directions, respectively. Y_f is the mass fraction of fuel. The diffusion velocity components, $\hat{u}$ and $\hat{v}$ are calculated by Fick's law:

$$Y_f \hat{u}_f = -D \frac{\partial Y_f}{\partial x} \tag{2a}$$

$$Y_f \hat{v}_f = -D \frac{\partial Y_f}{\partial y} \tag{2b}$$

where D is the mass diffusivity of fuel in the gas mixture. The molecular viscosity μ is calculated by the use of Sutherland's law (see Ref. 12), and the Lewis number $Le = 1$ is assumed to calculate the mass diffusivity D. In numerical calculations, the preceding governing equations are nondimensionalized by the freestream conditions, that is, velocity components by u_∞, density by ρ_∞, pressure by $\rho_\infty u_\infty^2$, and the total energy by $\rho_\infty u_\infty^2$. The subscript ∞ denotes the freestream condition. The cavity depth d is used as the length scale, and the timescale is d/u_∞.

III. CESE Method

The CESE method is a novel numerical framework for high-fidelity solution of hyperbolic conservation laws. Originally developed in Refs. 13–18, the tenet of the CESE method is a unified treatment of space and time in calculating flux balance. In contrast to modern upwind schemes, no Riemann solver and/or reconstruction procedure is used as the building block of the CESE method. As a result, the logic and computational counts of the CESE method are simpler and more efficient. Based on the CESE method, computer programs for solving unsteady flows in one, two, and three spatial dimensions for structured and unstructured meshes, and for meshes composed of mixed elements, have been developed. These solvers have been parallelized based on domain decomposition in conjunction with the use of message passing interface (MPI). Because no Riemann solver is used, we have straightforwardly extended the CESE method for flows with complex physical processes, including detonation, cavitations, and magnetohydrodynamics (MHD).

Previously, various flow phenomena were calculated by the use of the CESE method. In particular, the CESE solver is capable of calculating high-speed compressible flow as well as flows at very low Mach numbers without applying preconditioning to the governing equations. The CESE method is indeed an all-speed solver. Moreover, the CESE method is capable of simultaneously capturing strong shock waves and the acoustic waves in the same computational domain, despite that the amplitude of the pressure jump across the shock wave would be several orders of magnitude higher than that of the acoustic waves.

The CESE method employed in the present paper is based on the use of quadrilateral cells on the x–y plane,[17] which was extended from the original CESE method. Note that the original CESE method for two-dimensional flows was designed based on the use of triangular cells. In the present paper, a brief discussion of this particular extension of the CESE method is provided. The discussions here will be focused on the space–time geometry of the CESE method. We remark that the basic structure of the CESE method can always be easily grasped by visualization of the space–time geometry of conservation element (CE), solution element (SE), and how they facilitate the space–time integration. The detailed algebraic equations of the method, perhaps, only reaffirm the structure of the method. We refer the interested readers to the cited references for all details.

To proceed, let E_3 denote a three-dimensional Euclidean space, in which $x_1 = x$, $x_2 = y$, and $x_3 = t$. Let $\nabla \cdot$ be the divergence operator in E_3, and $h_m \overset{\text{def}}{=} [(f - f_v)_m, (g - g_v)_m, u_m]$ for $m = 1, 2, 3, 4$, and
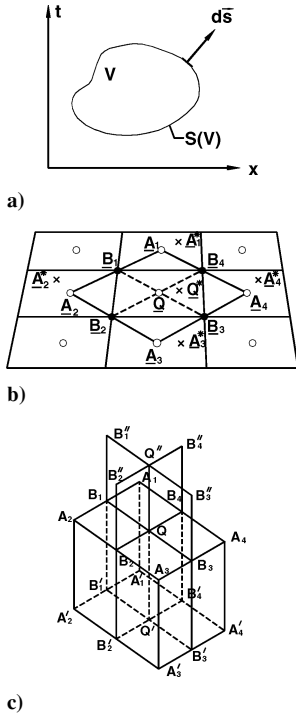
Fig. 1   Space–time geometry of the CESE method: a) surface element on boundary $S(V)$ of a region V, b) grid points on the x–y plane, and c) SEs and CEs.

5. Here $(f - f_v)_m$, $(g - g_v)_m$, and u_m are the mth components of $\mathbf{F} - \mathbf{F}_v$, $\mathbf{G} - \mathbf{G}_v$, and U, respectively, in Eq. (1). Aided by the preceding definition, for each $m = 1, 2, \ldots, 5$, the flow equations (1) become

$$\nabla \cdot \mathbf{h}_m = 0 \tag{3a}$$

Apply Gauss's divergence theorem to Eq. (3a) and we get

$$\oint_{S(V)} \mathbf{h}_m \cdot \mathrm{d}\,\mathbf{s} = 0 \tag{3b}$$

As shown in Fig. 1a, $S(V)$ is the boundary of the space–time region V in E_3 and $\mathrm{d}\mathbf{s}$ is a surface element vector pointing outward. Equation (3b) states that the total space–time flux $\mathbf{h}_m$, leaving volume V through $S(V)$, vanishes. All mathematical operations can be carried out as though E_3 were an ordinary three-dimensional Euclidean space. The CESE method is designed to integrate Eq. (3b) accurately to provide high-fidelity results of evolving u_m in the space–time domain.

The CESE method is a family of numerical schemes, with the *a* scheme[13] as its backbone. In contrast to conventional finite volume methods, the CESE method has separate definitions of CE and SE in the construction of the discretized equations for integration of Eq. (3b) in the space–time domain. CEs are nonoverlapping space–time subdomains such that 1) the whole computational domain can be filled by the CEs, 2) flux conservation can be enforced over each CE and/or over a union of several neighboring CEs, and 3) flow discontinuity is allowed inside a CE. On the other hand, SE are nonoverlapping space–time subdomains such that 1) SE do not generally coincide with a CE, 2) the union of all SEs does not have to fill the whole computational domain, 3) flow variables and fluxes are discontinuous across interfaces of neighboring SEs, and 4) within a SE, flow variable and flux function are assumed continuous, and they are approximated by the use of a prescribed smooth function. In the present paper, a first-order Taylor series expansion is used. Thus, the discretized flow variables and fluxes are linearly distributed inside each SE.

The time-marching strategy in the CESE method is designed based on a space–time staggered mesh stencil composed of CEs

and SEs. Note that when Eq. (3b) is integrated over the boundary of a CE, the surface element of $S(V)$ in Eq. (3b) is always lying inside a SE, where flow variables and fluxes are continuous. We remark that the paradigm of the Godunov schemes is that one has to resort to the use of a Riemann solver to reckon the nonlinear flux function at the cell interfaces. In the CESE method, however, flow information propagates only in one direction across all cell interfaces, that is, toward the future. Thus, the space–time flux integration can be straightforwardly carried out without reconciling the values of flux functions at cell interfaces through the use of a Riemann solver. In other words, in contrast to the upwind methods, there is no cell interface across which two-way flow traffic information propagates. Thus, the CESE method can capture shocks without using a Riemann solver. In what follows, we discuss specific space–time geometry of the CE and SE in the integration of Eq. (3b).

Consider Fig. 1b. The x–y plane is divided into nonoverlapping quadrilaterals. Two neighboring quadrilaterals share a common side. Vertices and centroids of quadrilaterals are marked by dots and circles, respectively. Q is the centroid of the quadrilateral $B_1B_2B_3B_4$. A_1, A_2, A_3, and A_4, respectively, are the centroids of the four quadrilaterals neighboring the quadrilateral $B_1B_2B_3B_4$. Q^*, marked by a cross in Fig. 1b, is the centroid of the polygon $A_1B_1A_2B_2A_3B_3A_4B_4$. Hereafter, point Q^*, which generally does not coincide with point Q, is referred to as the solution point associated with Q. Note that points A_1^*, A_2^*, A_3^*, and A_4^*, which are also marked by crosses, are the solution points associated with the centroids A_1, A_2, A_3, and A_4, respectively.

To proceed, we consider Fig. 1c. Here $t = n\Delta t$ at the nth time level, where $n = 0, \frac{1}{2}, 1, \frac{3}{2}$, etc. For a given $n > 0$, Q, Q', and Q'', respectively, denote the points on the nth, the $(1 - \frac{1}{2}n)$th, and the $(1 + \frac{1}{2}n)$th time levels with point Q being their common spatial projection. Other space-time mesh points, such as those shown in Fig. 1c, and also those not depicted, are defined similarly. In particular, Q^*, A_1^*, A_2^*, A_3^*, and A_4^* lie on the nth time level, and they are the space–time solution mesh points associated with points Q, A_1, A_2, A_3, and A_4. $Q'^*, A_1'^*, A_2'^*, A_3'^*$, and $A_4'^*$ lie on the $(1 - \frac{1}{2}n)$th time level and are the space–time solution mesh points associated with points Q', A_1', A_2', A_3', and A_4'.

With the preceding preliminaries, we are ready to discuss the geometry of the CE and SE associated with point Q^*, where the numerical solution of the flow variables u_m at nth time level are calculated based on the known flow solution in all points at an earlier time level, that is, $n - \frac{1}{2}$, denoted by superscript prime. First, the SE of point Q^*, denoted by $\mathrm{SE}(Q^*)$, is defined as the union of the five plane segments $Q'Q''B_1''B_1'$, $Q'Q''B_2''B_2'$, $Q'Q''B_3''B_3'$, $Q'Q''B_4''B_4'$, and $A_1B_1A_2B_2A_3B_3A_4B_4$ and their immediate neighborhoods.

To integrate Eq. (3b), four basic conservation elements (BCEs) of point Q^* are constructed, and they are denoted by $\mathrm{BCE}_l(Q)$, with $l = 1, 2, 3$, and 4. These four BCEs are defined to be the space–time cylinders $A_1B_1QB_4A_1'B_1'Q'B_4'$, $A_2B_2QB_1A_2'B_2'Q'B_1'$, $A_3B_3QB_2A_3'B_3'Q'B_2'$, and $A_4B_4QB_3A_4'B_4'Q'B_3'$, respectively. In addition, the compounded CE of point Q, denoted by $\mathrm{CE}(Q)$, is defined to be the space–time cylinder $A_1B_1A_2B_2A_3B_3A_4B_4A_1'B_1'A_2'B_2'A_3'B_3'A_4'B_4'$, that is, the union of the four preceding BCEs.

To proceed, the set of the space–time mesh points whose spatial projections are the centroids of quadrilaterals depicted in Fig. 1b is denoted by Ω, and the set of the space–time mesh points whose spatial projections are the solution points depicted in Fig. 1b is denoted by Ω^*. Note that the BCEs and the compounded CEs of any mesh point $\in \Omega$ and the SE of any mesh point $\in \Omega^*$ are defined in a manner identical to that described earlier for point Q and Q^*. With the clear definitions of the CE and SE as stated, the numerical integration of the space–time flux balance, that is, Eq. (3b), in the present modified CESE method can be summarized as follows:

1) For any $Q^* \in \Omega^*$ and $(x, y, t) \in \mathrm{SE}(\Omega^*)$, the flow variables and flux vectors, that is, $u_m(x, y, t)$, $f_m(x, y, t)$, and $g_m(x, y, t)$, are approximated to their numerical counterparts, that is, $u_m^*(x, y, t)$, $f_m^*(x, y, t)$, and $g_m^*(x, y, t)$, by the use of the first-order Taylor series expansion with respect to Q^* (x_{Q^*}, y_{Q^*}, t^n). Thus, the space–time flux vector $\mathbf{h}_m(x, y, t)$, can be replaced by $\mathbf{h}_m^*(x, y, t; Q^*)$, and the

numerical analog of Eq. (3b) for each $m = 1, 2, \ldots, 5$, is

$$\oint_{S[CE(Q)]} \boldsymbol{h}_m^* \cdot \mathrm{d}\boldsymbol{s} = 0 \qquad (4)$$

Equation (4) states that the discretized total flux of $\boldsymbol{h}_m^*$, leaving CE(Q) through its boundary, vanishes. We note that Eq. (4) can be written in terms of independent discrete solution variables that are the main flow variables and their spatial derivatives, $(u_{mx})_{Q^*}$ and $(u_{my})_{Q^*}$ in this approximation process.

2) When the integration of Eq. (4) is conducted over the $CE = BCE_1 + BCE_2 + BCE_3 + BCE_4$, the discrete flow variables $(u_m)_{Q^*}$ associated with the space–time point Q^* can be straightforwardly evaluated. This is achieved by the aid of the geometrical information of CE(Q^*) as shown in Fig. 1, and the linear distribution of $(u_m)_{Q^*}$ in each SE due to the adopted first-order Taylor series expansion for the flow variables inside the SE as the discretization process.

3) The calculation of the gradient variables, that is, $(u_{mx})_{Q^*}$ and $(u_{my})_{Q^*}$ is based on a finite difference approach in conjunction with the standard CESE artificial damping functions, that is, the a-ε-α scheme, in which parameter ε is associated with the overall damping effect and α is for shock capturing. In contrast to the original CESE method, the calculation of $(u_{mx})_{Q^*}$ and $(u_{my})_{Q^*}$ has nothing to do with the space–time flux conservation.

To calculate unsteady flows, the nonreflecting boundary condition treatment is critically important. Without an effective treatment, the reflected waves would inevitably contaminate the evolving flow solutions. Numerical treatments to achieve nonreflecting boundary conditions in the setting of conventional computational fluid dynamics (CFD) methods have been actively researched for a long time. In general, most of treatments were developed based on theorems of the partial differential equation, and they could be categorized into the following three groups: 1) application of the method of characteristics to the discretized equations, 2) use of the buffer zone or a perfectly matched layer, and 3) application of asymptotic analytical solution at the far field.

When the CESE method is set, we are only concerned with the integral equation. The preceding ideas of treating a nonreflective boundary are not applicable. Instead, the nonreflecting boundary condition treatments when the CESE method is set are based on flux conservation in the vicinity of the computational boundary.[18] In other words, the present nonreflecting boundary condition treatment is equivalent to letting the incoming flux from the interior domain to the boundary CE smoothly exit to the exterior of the domain. In the setting of the CESE method, the numerical implementation of this flux-based method is extremely simple because all flow information must propagate into the future. Chang et al.[18] have provided detailed discussions of various implementations of the preceding principle. It has been demonstrated that only negligible reflection occurs when a shock passes through the domain boundary. Moreover, along a wall boundary, a unified boundary condition for viscous flows is used. Based on local space–time flux conservation, a no-slip condition will be automatically enforced when the viscosity is not null. Again, the basic principle is based on the space–time flux conservation over CEs near the computational boundary.

IV. Results and Discussion

Three sets of numerical results are presented: 1) supersonic cavity flow in the supersonic combustion facility by Gruber et al.[1,2] and by Baurle et al.,[3] 2) Stalling and Wilcox's cavity flow test,[19] and 3) cavity flows with fuel injection. The first test is performed to assess the numerical accuracy of the calculated frequencies. The results will be compared with previously reported data and Rossiter's empirical relation (see Ref. 6). The second test is performed to assess the numerical accuracy of time-averaged amplitudes of pressure fluctuations along the cavity walls. The results will be compared with the experimental data.[19] In the third test, cavity flows with downstream, as well as upstream, injections are simulated. We will show that a cavity flow with a downstream transverse injection can
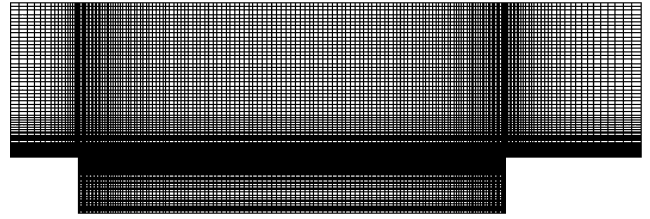

Fig. 2 Schematic of the computational domain and mesh; one mesh line is drawn for every five to show the clustered mesh points.

effectively generate strong vortices and acoustic waves for fuel/air mixing enhancement.

A. Frequency Calculations

The first numerical example follows the testing condition in the U.S. Air Force Research Laboratory supersonic combustion facility reported in Refs. 1, 2, and 5. A supersonic flow at Mach 2 and Reynolds number of 4×10^5 passes a swallow cavity with $L/d = 7.76$, where L and D are the length and depth of the cavity, respectively. The computational domain outside of the cavity is $0 \leq x \leq 11.52$, and $0 \leq y \leq 3.82$, where x and y are nondimensionalized by d. Mesh points were clustered at the forward and aft bulkheads, at the plane spanning over the cavity mouth, and along the lateral sidewalls of the cavity. There were 143,000 quadrilateral elements used for the computational domain. Figure 2 shows the mesh, in which one of every five mesh lines is displayed. The nonreflecting boundary condition is applied to the freestream surfaces and outlet. Initially, velocities inside the cavity are set to zero, and the density and pressure of the whole domain are set to the freestream values. The time step was chosen such that the Courant–Friedrichs–Lewy number (CFL) ≈ 0.8 based on the freestream condition.

Figure 3 shows a series of snapshots of pressure contours, vorticity contours, and numerical schlieren images that are contour plots of

$$|\nabla \rho| = \sqrt{\left(\frac{\partial \rho}{\partial x}\right)^2 + \left(\frac{\partial \rho}{\partial y}\right)^2} \qquad (5)$$

Figures 3 demonstrate very complex flow features, including traveling acoustic waves, vortex generation at the leading edge, shedding vortices in the free shear layer, and pressure waves impinging on and rebounding from the aft wall. The interactions between the rebounding pressure waves and shed vortices form a feedback loop that leads to self-sustained oscillations as illustrated by Rossiter (see Ref. 6). In Fig. 3b, periodic shear layer deflections in the transverse direction could be clearly discerned. Inward deflection results in mass addition into the cavity; outward deflection expels mass from the cavity. This periodic mass addition/expulsion mechanism enhances fuel/air mixing. Moreover, flapping shock/expansion waves emanating from the upstream bulkhead of the cavity, shown in Fig. 3c, can also enhance fuel/air mixing.

Figure 4 shows pressure histories on the aft wall and on the floor. The flow has reached a self-sustained oscillatory state after about $15t_c$, where $t_c = D/U_\infty$. However, the oscillation pattern changes from cycle to cycle, and we cannot clearly identify the period of the oscillation cycles. This is consistent with experimental observation reported in Ref. 20. The amplitude of the pressure oscillations at the aft wall is much higher than that at the cavity floor due to the mass addition/expulsion mechanism near the aft wall. Figure 5 shows the frequency spectra of the pressure data in Fig. 4. The predicted values of the dominant frequencies compare well with the Rossiter relation (see Ref. 6) and the numerical results by Baurle et al.[3] The Rossiter formula is

$$f_m = \left(\frac{U}{L}\right) \frac{m - \alpha}{(K)^{-1} + M_\infty (T/T_o)^{\frac{1}{2}}} \qquad (6)$$

where f_m is the resonant frequency corresponding to the mth mode, U is the main stream velocity, L is the cavity length, $\alpha = 0.513$,
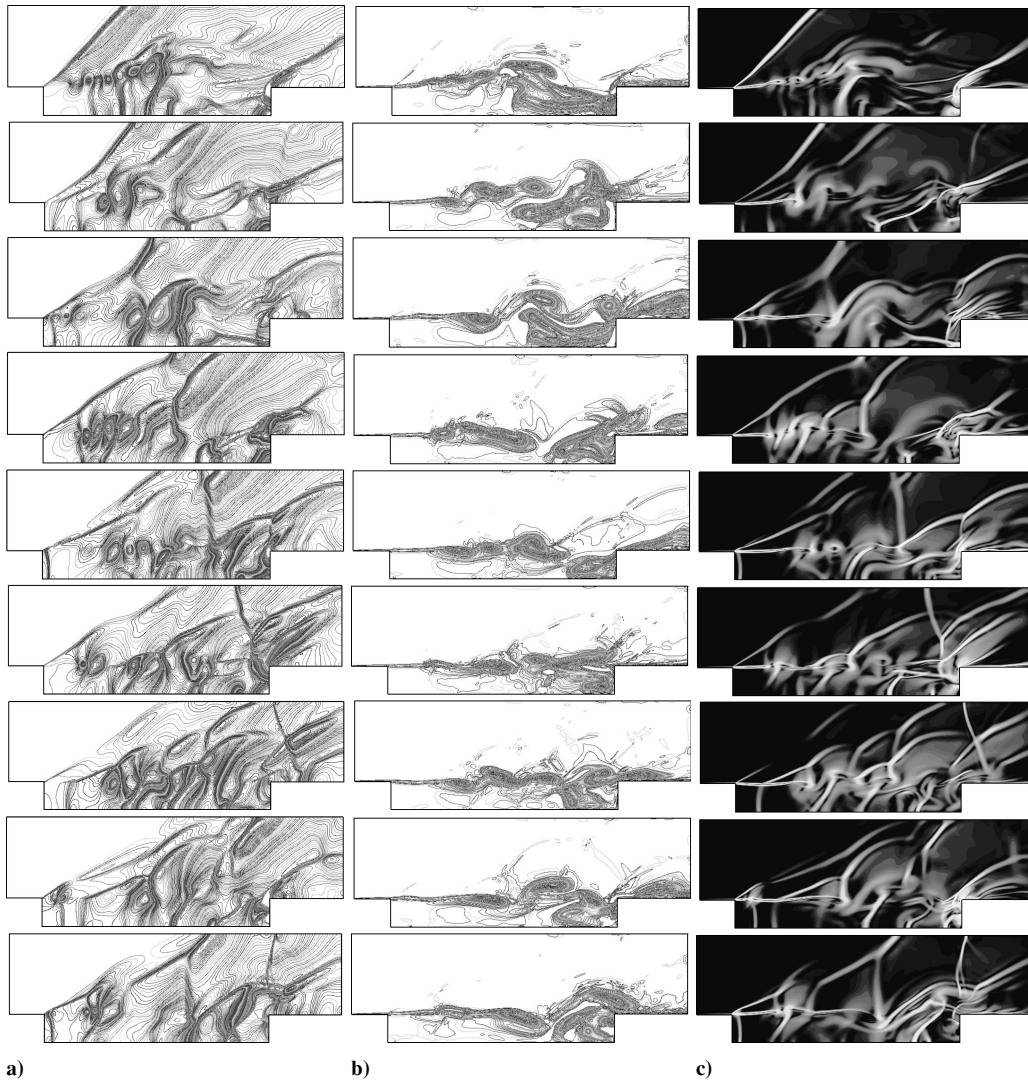
Fig. 3   Snapshots of flowfields of a cavity flow with $M = 2.0$ and $L/D = 7.76$ at nine different times ($\Delta t = 0.8t_c$): a) pressure contours, b) vorticity contours, and c) numerical schlieren images.

and $K = 0.57$ (Ref. 5). Figure 5 shows five calculated dominant frequencies, that is, 2523, 3533, 4290, 5804, and 8579 Hz, that compare well with the third, fourth, fifth, sixth, and ninth modes predicted by the Rossiter relation. The first and second frequency modes also compared well with Baurle's calculation.

To proceed, we perform simulation of the same cavity flow with an added transverse injection at upstream of the cavity. The freestream flow condition and the cavity geometry are identical to that shown in Figs. 3–5. The injection jet opening is $0.2\,D$, and its center is located $1.0\,D$ upstream from the leading edge of the cavity. A choked jet with a uniform condition at the opening is imposed:

$$J = 1.0, \qquad p_j/p_\infty = 4.34, \qquad \rho_j/\rho_\infty = 6.593$$

where the subscript j denotes the injection stream and J is the ratio of the stream momentum flux of the injected jet as compared to the freestream:

$$J = (\rho u^2)_{\text{jet}}/(\rho u^2)_{\text{freestream}} \qquad (7)$$

Figures 6a and 6b show snapshots of pressure and vorticity contours, respectively, at three different times with time increment $\Delta t = 0.75t_c$. Compared to Fig. 3a, pressure contours in Fig. 6a are smoother and less violent due to the blocking effect provided by the transverse injection upstream of the cavity. Compared to Fig. 3c, Fig. 6 shows a much thicker shear layer spanning over the cavity mouth. It is evident that vortex shedding and periodic transverse

deflections of the separated shear layer have been significantly suppressed. Moreover, Fig. 6b shows only one major vortex trapped inside the cavity, and there is little evidence for the existence of periodic mass addition/expulsion mechanism.

Figure 7 shows the frequency spectrum of pressure oscillations on the aft wall, where $y = 0.75D$. When the injection is applied, flow oscillations inside the cavity are suppressed, and the oscillation pattern is changed. The calculated dominant frequencies here are 1893, 2523, and 3470 Hz. This result is qualitatively consistent with that reported by Vakili and Gauthier.[9] As compared to that in Fig. 5 for the same cavity flow without injection, the dominant frequencies shift to lower values due to the upstream injection. Although not shown, the averaged amplitudes of pressure oscillations are reduced to about 25–30% of that shown in Fig. 4 for the same cavity flow without upstream injection.

B.   Pressure Amplitude Calculation

Because the oscillation patterns in cavity flows change from cycle to cycle, it is difficult to compare the numerical results with the experimental data in terms of the instantaneous pressure oscillations. In Sec. IV.A, we have assessed the numerical accuracy of calculated frequency of pressure oscillations inside the cavity based on the use of Gruber's testing conditions. To further validate the numerical accuracy of the calculated amplitudes of pressure oscillations, we use the time-averaged experimental data reported by Stallings and Wilcox.[19] In this case, a freestream at Mach 1.5 flows over an open cavity with $L/D = 6.0$. Figure 8 shows the comparison between

the present numerical solutions and the experimental data for the time-averaged pressure coefficient, which is defined as

$$c_p = 2\left[\bar{p} - \left(1/\gamma M_\infty^2\right)\right] \qquad (8)$$

where $\bar{p}$ is the time-averaged surface pressure. The calculated results are in favorable agreement with the experimental data, except near the fore wall of the cavity. The discrepancy between the numerical solution and experimental data is perhaps due to uncertainties of
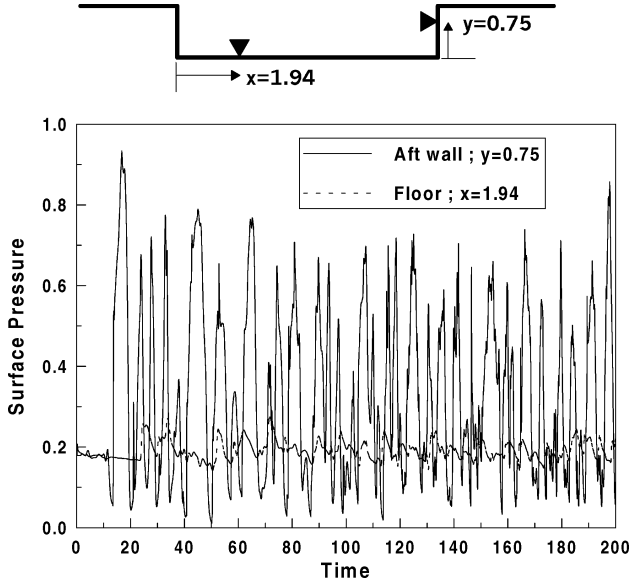

Fig. 4   Monitored pressure history on the wall.
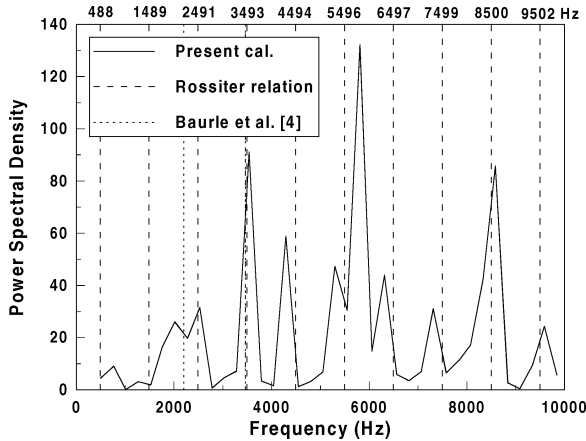
Fig. 5   Calculated dominant frequencies of the U.S. Air Force Research Laboratory testing case.
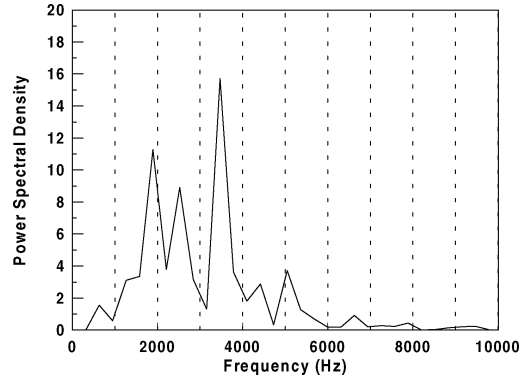

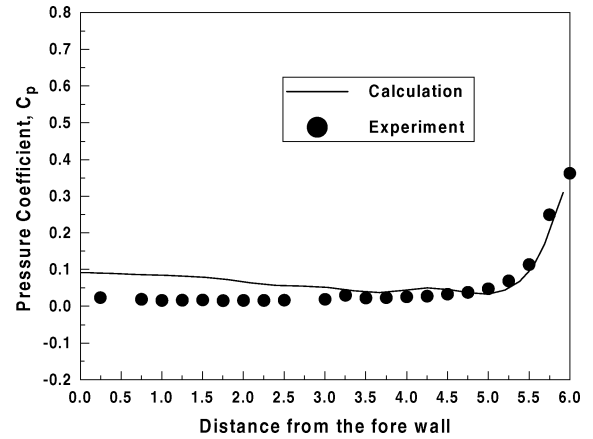**Fig. 7   Dominant frequencies for the cavity flow with injection.**

Fig. 8   Time-averaged pressure coefficients along the cavity floor in the NASA testing case.
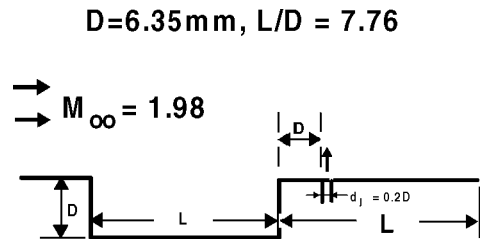
$$D=6.35\,mm,\ L/D = 7.76$$

$$M_{oo} = 1.98$$

Fig. 9   Schematic diagram of flowfield inside a supersonic-combustion duct.

a)   b)
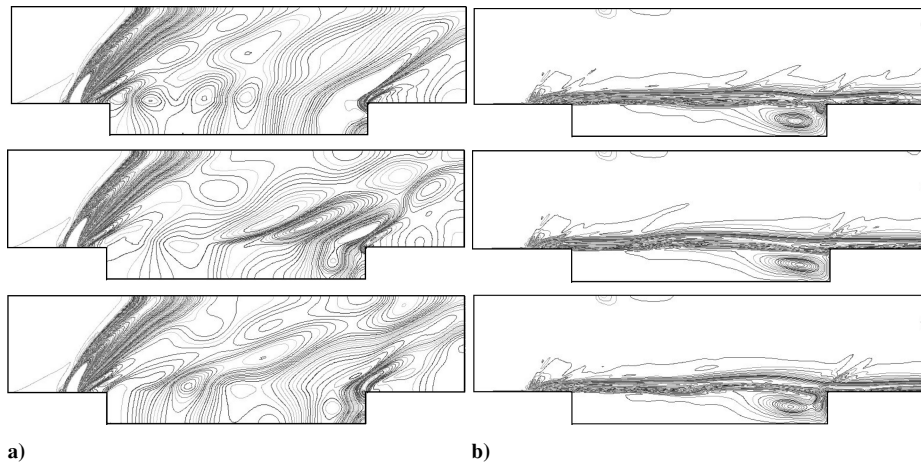
Fig. 6   Cavity flow with an upstream injection; $J = 1$, $M = 2.0$, and $L/D = 7.76$: a) snapshots of pressure contours and b) snapshots of vorticity contours.
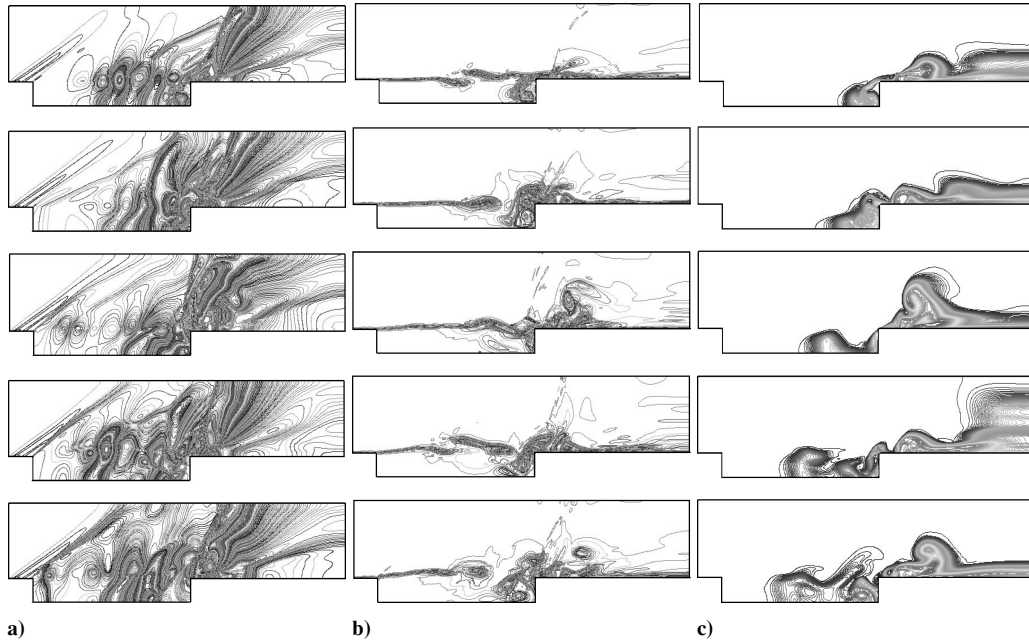
Fig. 10 Snapshots of flowfields of a cavity flow with downstream injection: a) pressure contours, b) vorticity contours, and c) mole fraction contours of fuel.
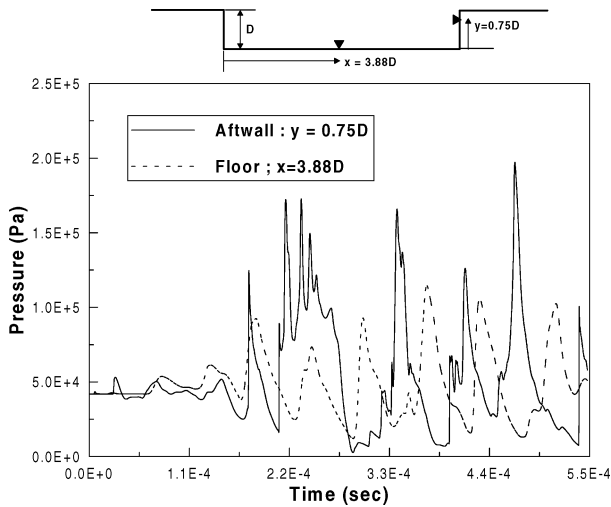

Fig. 11 Pressure oscillations on the cavity wall of an open cavity with downstream injection.

the incoming boundary layer in the experiments. It can also be due to the two-dimensional assumption employed in the present paper. The same issue has been discussed by Rizzetta.[8]

C. Cavity for Fuel/Air Mixing Enhancement

Results in Sec. IV.A. show that fuel injection upstream of a cavity suppresses instability of cavity flows and, thus, is not favorable to be used for fuel/air mixing enhancement in the setting of a scramjet engine combustor. To proceed, we simulate a cavity flow with a downstream transverse injection. The cavity geometry and cavity flow conditions are identical to that reported by Gruber et al.[21] A supersonic flow at Mach 1.98 ($P_\infty = 41.8$ kPa and $\rho_\infty = 0.860$ kg/m^3) passes a cavity with $L/D = 7.76$ with $D = 6.35$ mm. In the present calculation, hydrogen is the injected fuel. The size and position of the injection jet opening are shown in Fig. 9. A choked jet with a uniform condition at the opening is imposed with the following flow conditions: $J = 1.0$, $u_j = 317$ m/s, $P_j = 16.4$ kPa, $\rho_j = 2.283$ kg/m^3.

Figure 10 shows snapshots of pressure, vorticity, and fuel mass fraction contours at five different times with time increment $\Delta t = 15$ μs. These contour plots show violent interactions between

the fuel jet and the cavity flow, leading to complex pressure waves and large vortex structures around the aft wall of the cavity and the fuel injection slot. Compared to the feedback mechanism in cavity flows without any injection, the self-sustained flow oscillations here are much more violent. As a result, the mass addition/expulsion process near the aft bulkhead of the cavity has been greatly enhanced by the fuel injection downstream of the cavity. Moreover, these enhanced oscillations near the aft corner cause part of fuel, which was injected downstream of the cavity, to move upstream, enter into the cavity and become trapped in recirculation bubbles. Thus, the flow residence time of the fuel in the combustion chamber significantly increases and flameholding characteristics could be improved.

Figure 11 shows the time histories of calculated pressures at two locations inside the cavity, that is, the center of the cavity floor and near the corner on the aft wall, indicated by filled triangles in Fig. 11. The flow reaches a self-sustained oscillatory state after about 200 μs ($\cong 16t_c$). Contrary to the case of the cavity flow with an upstream injection (refer to Fig. 6), downstream injection here enhances the overall pressure oscillations of the flowfield with much higher pressure oscillation amplitudes. Moreover, the amplitudes of the pressure oscillations on the floor and on the aft bulkhead are comparable, whereas, in the case without fuel injection, the pressure fluctuation amplitudes are much larger on the aft bulkhead than that on the cavity floor.

V. Conclusions

In the present paper, we applied the CESE method to simulate supersonic cavity flows in the setting of a dual-mode ramjet/scramjet engine. Two-dimensional Navier–Stokes solvers are solved for three sets of testing conditions. As part of the code validation effort, the calculated results showed that the CESE method could vividly capture the well-known feedback mechanism and the self-sustained oscillations in the supersonic cavity flows. We observed cycle-to-cycle changes in oscillation patterns. The calculated frequencies of pressure oscillations at locations inside the cavity compared well with Rossiter's relation (see Ref. 6) and the Baurle et al.[3] data. Numerical accuracy is further validated by favorable comparison between the calculated amplitudes of pressure oscillations along cavity floor and the experimental data by Stallings and Wilcox.[19]

With regard to mixing and flameholding enhancement for supersonic combustion, our results show that an upstream injection drastically suppresses flow oscillations. The dominant frequencies

of pressure oscillations shift to lower values with much lower amplitudes. Moreover, upstream injection induces thicker and more stable free shear layer spanning over the cavity mouth, leading to vortex motions reduced drastically. In general, upstream injection suppresses the desired mixing and flameholding features for supersonic combustion. On the other hand, cavity flows with a downstream injection show promising potential for mixing and flameholding enhancement. Because of interactions between flow oscillations near the aft bulkhead of the cavity and the injection jet, the amplitudes of the pressure oscillations are greatly amplified as compared to the case without injection. Large vortices occur, leading to fuel propagation upstream in to the cavity, where the recirculation bubbles are highly unstable. They interact with the pulsating vortex structure downstream of the cavity. The preceding results warrant further investigation of the fuel injection downstream of an open cavity for possible fuel/air mixing and flameholding enhancement. In general, numerical results obtained by the CESE method can effectively capture the unsteady and complex mixing processes of cavity flows in the setting of an advanced scramjet engine.

Acknowledgments

References

[1]Gruber, M. R., Baurle, R. A., Mathur, T., and Hsu, K.-Y., "Fundamental Studies of Cavity-Based Flame Holder Concepts for Supersonic Combustors," *Journal of Propulsion and Power*, Vol. 17, No. 1, 2001, pp. 146–153.

[2]Gruber, M. R., Jackson, K., Mathur, T., and Billig, F., "Experiments with a Cavity-Based Fuel Injector for Scramjet Applications," International Society of Air-Breathing Engines, ISABE Paper IS-7154, Sept. 1999.

[3]Baurle, R. A., Tam, C.-J., and Dasgupta, S., "Analysis of Unsteady Cavity Flows for Scramjet Applications," AIAA Paper 2000-3617, July 2000.

[4]Yu, K. H., Wilson, K. J., and Schadow, K. C., "Effect of Flame-Holding Cavities on Supersonic-Combustion Performance," *Journal of Propulsion and Power*, Vol. 17, No. 6, 2001, pp. 1287–1295.

[5]Ben-Yakar, A., and Hanson, R. K., "Cavity Flame-Holders for Ignition and Flame Stabilization in Scramjets: An Overview," *Journal of Propulsion and Power*, Vol. 17, No. 4, 2001, pp. 869–877.

[6]Tam, C. K. W., and Block, P. J. W., "On the Tones and Pressure Oscillations Induced by Flow over Rectangular Cavities," *Journal of Fluid Mechanics*, Vol. 89, Pt. 2, 1978, pp. 373–399.

[7]Rockwell, D., and Naudascher, E., "Review–Self-Sustaining Oscillations of Flow past Cavities," *Journal of Fluids Engineering*, Vol. 100, June 1978, pp. 152–165.

[8]Rizzetta, D. P., "Numerical Simulation of Supersonic Flow over a Three-Dimensional Cavity," *AIAA Journal*, Vol. 26, No. 7, 1988, pp. 799–807.

[9]Vakili, A. D., and Gauthier, C., "Control of Cavity Flow by Upstream Mass-Injection," *Journal of Aircraft*, Vol. 31, No. 1, 1994, pp. 169–174.

[10]Sarno, R. L., and Franke, M. E., "Suppression of Flow-Induced Pressure Oscillations in Cavities," *Journal of Aircraft*, Vol. 31, No. 1, 1994, pp. 90–96.

[11]Lamp, A. M., and Chokani, N., "Computation of Cavity Flows with Suppression Using Jet Blowing," *Journal of Aircraft*, Vol. 34, No. 4, 1997, pp. 545–551.

[12]Anderson, D. A., Tannehill, J. C., and Pletcher, R. H., *Computational Fluid Mechanics and Heat Transfer*, McGraw–Hill, New York, 1984, p. 189.

[13]Chang, S.-C., "The Method of Space–Time Conservation Element and Solution Element—A New Approach for Solving the Navier–Stokes and Euler Equations," *Journal of Computational Physics*, Vol. 119, 1995, pp. 295–324.

[14]Chang, S.-C., Yu, S.-T., Himansu, A., and Wang, X.-Y., "The Method of Space–Time Conservation Element and Solution Element—A New Paradigm for Numerical Solution and Conservation Laws," *Computational Fluid Dynamics Review 1998*, edited by M. Hafez and K. Oshima, World Scientific, London, 1999, pp. 206–240.

[15]Chang, S.-C., Wang, X.-Y., and Chow, C.-Y., "The Space–Time Conservation Element and Solution Element Method: A New High-Resolution and Genuinely Multidimensional Paradigm for Solving Conservation Laws," *Journal of Computational Physics*, Vol. 156, 1999, pp. 89–136.

[16]Chang, S.-C., Wang, X.-Y., and To, W.-M., "Application of the Space–Time Conservation Element and Solution Element Method to One-Dimensional Convection–Diffusion Problem," *Journal of Computational Physics*, Vol. 165, 2000, pp. 189–215.

[17]Zhang, Z. C., Yu, S.-T. J., and Chang, S. C., "A Space–Time Conservation Element and Solution Element Method for Solving the Two- and Three-Dimensional Euler Equations by Quadrilateral and Hexahedral Meshes," *Journal of Computational Physics*, Vol. 175, No. 1, 2002, pp. 168–199.

[18]Chang, S.-C., Himansu, A., Loh, C. Y., Wang, X.-Y., Yu, S.-T., and Jorgenson, P. C. E., "Robust and Simple Non-Reflecting Boundary Conditions for the Space-Time Conservation Element and Solution Element Method," AIAA Paper 97-2077, June–July 1997.

[19]Stallings, R. L., Jr., and Wilcox, F. J., "Experimental Cavity Pressure Distributions at Supersonic Speeds," NASA TP-2683, June 1987.

[20]Lin, J.-C., and Rockwell, D., " Organized Oscillations of Initially Turbulent Flow past a Cavity," *AIAA Journal*, Vol. 39, No. 6, 2001, pp. 1139–1151.

[21]Gruber, M. R., Nejad, A. S., Chen, T. H., and Dutton, J. C., "Compressibility Effects in Supersonic Transverse Injection Flow Fields," *Physics of Fluids*, Vol. 9, No. 5, 1997, pp. 1448–1461.

M. Sichel
Associate Editor